



# Interfacial Engineering of Reduced Graphene Oxide for Aramid Nanofiber-Enabled Structural Supercapacitors

Paraskevi Flouda,<sup>[a]</sup> Xueyan Feng,<sup>[b]</sup> James G. Boyd,<sup>[c]</sup> Edwin L. Thomas,<sup>[b]</sup> Dimitris C. Lagoudas,<sup>[a, c]</sup> and Jodie L. Lutkenhaus<sup>\*[a, d]</sup>

Structural energy storage systems can simultaneously store energy and bear mechanical loads and are emerging technologies for electric vehicles, aircrafts, and satellites since they offer significant mass and volume savings. However, many of the materials used in energy storage applications are not mechanically robust or, on the other hand, mechanically stiff materials are not necessarily electrochemically active. One solution is to combine reduced graphene oxide (rGO) sheets and aramid nanofibers (ANFs). Here we hypothesize that engineering the interfacial interactions between rGO sheets and the ANFs will lead to enhanced mechanical properties, as noncovalent interactions offer multiple sites for load transfer. rGO sheets are functionalized with carboxylic acid ( $-\text{COOH}$ ) and amine ( $-\text{NH}_2$ )

groups, and the effect on the mechanical and electrochemical performance of nanocomposite supercapacitor electrodes is investigated. Notably, the  $-\text{NH}_2$  functionalization and the addition of ANFs leads to a dramatic 200% improvement of the strength of the electrodes without significantly compromising the electrochemical performance. Furthermore, it is demonstrated that these electrodes' multifunctionality is superior to other state-of-the-art structural electrodes and may pose possible replacements for steel or epoxy. These findings provide critical knowledge for the design of next-generation multifunctional electrodes in that we highlight the importance of interfacial engineering.

## 1. Introduction

Structural energy storage has arisen as an urgent need to satisfy today's demands for lightweight vehicles, flexible electronics, and biometrics. Structural, flexible, or stretchable batteries and supercapacitors could potentially address both electrochemical and mechanical needs in a single unit, yielding savings in both mass and volume.<sup>[1]</sup> However, conventional batteries and supercapacitors fail to address these two functionalities and often rely on the use of external packaging for structural support.<sup>[2]</sup> The emergence of multifunctional electrodes provides a promising and reliable solution.<sup>[3]</sup> Recent studies on multifunctional electrodes and electrolytes for batteries and supercapacitors revealed a trade-off between the electrochemical and mechanical properties.<sup>[4]</sup> One possible

route to address this is by engineering the interface between the material components in the electrode. The proposed advantage is that the mechanical properties will be enhanced due to interfacial interactions without significantly sacrificing energy storage.<sup>[5]</sup> Therefore, understanding the role of the interface in this application is critical.

Aramid nanofibers (ANFs), a nanoscale version of Kevlar® fiber, are currently one of the most promising candidates as building blocks in such nanocomposite materials.<sup>[6]</sup> Kevlar®, a well-known para-aramid fiber consisting of poly(paraphenylene terephthalamide) (PPTA) chains, has been widely employed in structural applications due to its superior mechanical properties (Young's modulus of 144 GPa and tensile strength of 3.8 GPa).<sup>[7]</sup> These mechanical properties result from the rigid extended chain backbone and the  $\pi$ - $\pi$  stacking and hydrogen bonding interactions between the PPTA chains.<sup>[7]</sup> Recently Kotov et al. developed a method to fabricate ANFs by the dissolution of a macroscale bulk Kevlar® thread in dimethyl sulfoxide (DMSO) with potassium hydroxide (KOH).<sup>[6a]</sup> ANFs obtained by this method have diameters of 30–40 nm and lengths up to 10  $\mu\text{m}$ . This strategy enabled the incorporation of ANFs into nanocomposite materials as demonstrated in several studies.<sup>[8]</sup> As an example, ANFs used as reinforcement nanofillers in epoxy resin resulted in an enhancement in elastic modulus and toughness by 28% and 22%, respectively.<sup>[9]</sup> However, more recent studies have shifted to the incorporation of ANFs in composites for energy storage applications, such as in structural electrodes and separators for batteries and supercapacitors.<sup>[10]</sup>

Graphene, a two-dimensional honeycomb-like carbon lattice, is of great interest due to its exceptional properties, such as high electrical conductivity ( $\sim 10^6 \text{ S/cm}$ ), high surface area

[a] *P. Flouda, Prof. D. C. Lagoudas, Prof. J. L. Lutkenhaus  
Department of Materials Science and Engineering  
Texas A&M University  
College Station, TX 77843, United States  
E-mail: jodie.lutkenhaus@tamu.edu*

[b] *X. Feng, Prof. E. L. Thomas  
Department of Materials Science and NanoEngineering  
Rice University  
Houston, TX 77005, United States*

[c] *Prof. J. G. Boyd, Prof. D. C. Lagoudas  
Department of Aerospace Engineering  
Texas A&M University  
College Station, TX 77843, United States*

[d] *Prof. J. L. Lutkenhaus  
Department of Chemical Engineering  
Texas A&M University  
College Station, TX 77843, United States*

 Supporting information for this article is available on the WWW under <https://doi.org/10.1002/batt.201800137>

( $2630\text{ m}^2/\text{g}$ ) and excellent mechanical properties (Young's modulus of  $1.1\text{ GPa}$  for a graphene monolayer).<sup>[11]</sup> These properties established the use of reduced graphene oxide (rGO) a processable analogue of graphene not only for structural applications but also for energy storage applications.<sup>[12]</sup> Typically rGO sheets have lateral sizes of a few  $\mu\text{m}$  and thicknesses of  $1\text{ nm}$ .<sup>[13]</sup> There have been very few reports on rGO-containing composites for structural energy and power.<sup>[14]</sup> For example, rGO/polyaniline electrodes exhibited a tensile strength of  $12.6\text{ MPa}$  and a specific capacitance of  $233\text{ F/g}$ , whereas rGO/MnO<sub>2</sub> electrodes showed a tensile strength of  $8.8\text{ MPa}$  and an areal capacitance of  $897\text{ mF/cm}^2$ .<sup>[15]</sup>

To date, only a handful of studies on rGO/ANF-containing composites have been reported. rGO/ANF paper prepared by vacuum-assisted filtration exhibited a Young's modulus of  $30\text{ GPa}$  and a tensile strength of  $210\text{ MPa}$ .<sup>[8c]</sup> Moreover, the use of rGO/ANF as nanofillers in poly(methyl methacrylate) (PMMA) has also been reported, resulting in an increase in Young's modulus by 71%.<sup>[8b]</sup> Recently, our group demonstrated for the first time the fabrication of rGO/ANF nanocomposite electrodes for structural supercapacitors. This was facilitated, through two fabrication techniques, layer-by-layer (LbL) assembly and vacuum-assisted filtration.<sup>[16]</sup> In both cases the extensive hydrogen bonding and  $\pi$ - $\pi$  interactions between ANFs and rGO sheets were harnessed, resulting in high strength electrodes. A good combination of mechanical and electrochemical properties was achieved, with the incorporation of the ANFs leading to a 350% and 290% increase in Young's modulus and tensile strength, respectively, while only slightly reducing the capacitance.<sup>[16]</sup> Although encouraging, these results led us to speculate that the mechanical properties might be improved even further through engineering the interfacial interactions between rGO sheets and ANFs.

Here, we explore how functionalization (using  $-\text{COOH}$  and  $-\text{NH}_2$ ) of rGO sheets influences the mechanical and energy storage properties of rGO/ANF structural supercapacitor electrodes. ANFs and rGO sheets were selected as the structural components and rGO sheets were used as the electrochemically active component. These two components were processed into free-standing flexible electrodes using vacuum-assisted filtration, Figure 1. The hydrogen bonding interactions between the functional groups on the rGO and the ANFs were examined using X-ray photoelectron spectroscopy (XPS). Electrodes of three different compositions (0 wt %, 10 wt %, and 25 wt % ANF) were characterized using tensile testing, cyclic voltammetry, and galvanostatic cycling to evaluate the mechanical and

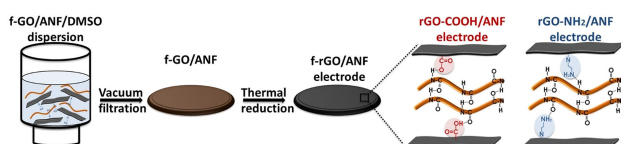


**Figure 1.** Fabrication of f-rGO/ANF composite electrodes. f-GO sheets were mixed with ANF in dimethylsulfoxide (DMSO), followed by vacuum filtration. The obtained f-GO/ANF electrodes were thermally reduced to yield f-rGO/ANF, where ANF interact with f-rGO through extensive hydrogen bonding and  $\pi$ - $\pi$  stacking interactions.

electrochemical properties. We discuss the results in the context of interfacial interactions and then compare the trade-off using a multifunctional efficiency metric. These results favorably demonstrate that interfacial interactions can indeed improve mechanical properties, while still maintaining electrochemical activity as compared to rGO paper electrodes.

## 2. Results and Discussion

### 2.1. Functionalization

Graphene oxide (GO) prepared by the modified Hummers method was first reduced with hydrobromic acid (HBr) to open the epoxide groups ( $-\text{O}-$ ) and convert them into hydroxyl groups ( $-\text{OH}$ ).<sup>[17]</sup> Subsequently, an esterification reaction took place by the introduction of oxalic acid that interacts with the  $-\text{OH}$  groups. The obtained functionalized GO (GO-COOH) contained  $-\text{COOH}$  not only on the edges but also on the basal planes.<sup>[18]</sup> For the second functionalization, graphene oxide was reacted with ethylenediamine. The amine groups of ethylenediamine chemically graft to GO (GO-NH<sub>2</sub>) via nucleophilic substitution reactions on the epoxide groups.<sup>[19]</sup> The carboxylic acid ( $-\text{COOH}$ ) and amine ( $-\text{NH}_2$ ) functionalizations lead to an increase in the d-spacing of the (002) reflection by  $\sim 1.7\%$  and  $\sim 14.6\%$ , respectively.<sup>[18,20]</sup>

Successful functionalizations were verified using Raman spectroscopy and XPS. Raman spectra of GO, GO-COOH, and GO-NH<sub>2</sub> are shown in Figure 2a. Characteristic D and G bands were observed at  $1352\text{ cm}^{-1}$  and  $1600\text{ cm}^{-1}$ , respectively. The D band is associated with defects leading to  $\text{sp}^3$  hybridized carbon atoms, whereas the G band arises from the in-plane bond stretching vibration of  $\text{sp}^2$ -hybridized carbon atoms.<sup>[21]</sup> The relative intensity of the two bands ( $I_{\text{D}}/I_{\text{G}}$ ) reveals the amount of disorder. The relative intensity  $I_{\text{D}}/I_{\text{G}}$  for GO was 1.09, while the

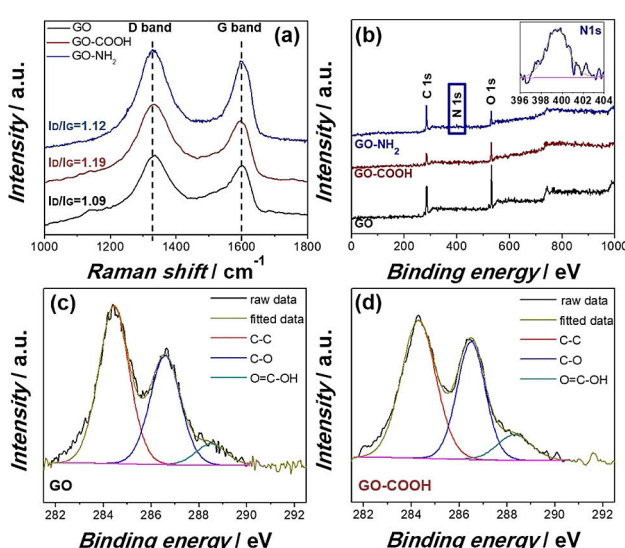


**Figure 2.** a) Raman spectra and b) XPS survey scans of GO, GO-COOH, and GO-NH<sub>2</sub>. The inset shows the high resolution N 1s peak for GO-NH<sub>2</sub>. High resolution XPS spectra for the C 1s peak for c) GO and d) GO-COOH.

value for GO-COOH rose to 1.19. The increase of the D/G ratio indicates the introduction of defects during -COOH functionalization.<sup>[22]</sup> The D/G ratio for GO-NH<sub>2</sub> also increased, but only slightly (1.12) indicating that ethylenediamine reacted with the epoxide groups on the surface of GO without significantly affecting the aromatic carbon-carbon bonds.<sup>[22]</sup>

Functionalization was also confirmed using XPS. Figure 2b illustrates the XPS survey scans of GO, GO-COOH, and GO-NH<sub>2</sub>. GO had 74 atomic percent (at%) carbon and 26 at% oxygen to yield a C/O ratio of 2.85. In GO-COOH the C/O ratio decreased to 2.20, whereas in GO-NH<sub>2</sub> the C/O ratio increased to 4.91, while an N 1s peak (2.5 at%) appeared at 399.9 eV (Figure 2b, inset), indicating the successful -NH<sub>2</sub> modification. Moreover, the C 1s XPS spectrum for GO (Figure 2c) shows three distinct peaks at 284.5, 286.6 and 288.7 eV attributed to sp<sup>2</sup>-hybridized carbon, C=O and -COOH groups, respectively.<sup>[23]</sup> GO-COOH (Figure 2d) and GO-NH<sub>2</sub> (Figure S1) also exhibited these three peaks. In GO-COOH, the peak attributed to the carboxylic acid groups (-COOH) slightly increased from 7.4% to 9.8% (Table S1), indicating the successful addition of the -COOH groups. From here, we generically term GO-NH<sub>2</sub> and GO-COOH as functionalized GO (f-GO).

## 2.2. Electrode Morphology

f-GO/ANF electrodes of varying compositions were fabricated using vacuum filtration, Figure 1. Desired amounts of ANF/DMSO and f-GO/DMSO dispersions were mixed and stirred together, followed by the addition of water and vacuum filtration. The addition of water serves to reprotoxinate the ANF amide bonds, leading to extensive hydrogen bonding with the oxygen-containing and/or the amine functional groups on f-GO.<sup>[24]</sup> Moreover, ANFs and f-GO interact with each other through  $\pi$ - $\pi$  interactions between ANF's aromatic rings and f-GO graphitic basal planes.<sup>[25]</sup>

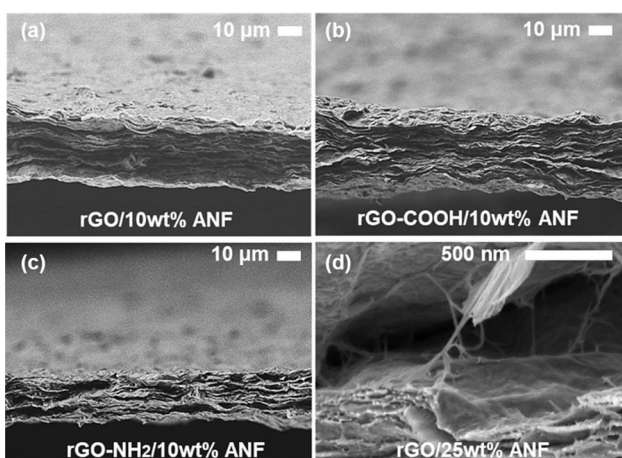


**Figure 3.** Low magnification cross-sectional SEM images of a) rGO/10 wt % ANF, b) rGO-COOH/10 wt % ANF, and c) rGO-NH<sub>2</sub>/10 wt % ANF. High resolution cross-sectional SEM image of d) rGO/25 wt % ANF after tensile testing. Both wavy rGO platelets and taut load bearing ~10 nm diameter ANF adhering and spanning the rGO layers are evident.

The as-prepared f-GO/ANF composite films were then reduced thermally at 200 °C under vacuum for 2 h to yield functionalized reduced graphene oxide (f-rGO). Cross-sectional SEM images of f-rGO/10 wt % ANF composite films revealed a highly layered and compact structure, Figure 3. The films containing functionalized rGO exhibited a slightly wavy morphology and had thicknesses varying from 8 to 15  $\mu$ m. ANFs were not directly observed from the cross-sectional SEM images due to their small size and low content. To observe the ANFs, high resolution cross-sectional SEM was conducted on rGO/25 wt % ANF films after tensile testing (Figure S2), Figure 3d, which shows ANFs spanning the fracture surfaces of the electrode. As shown later, ANFs spanning the lateral gaps between f-rGO sheets is perhaps one mechanism for the observed mechanical enhancement in rGO/ANF electrodes.

## 2.3. Reduction

Reduction was verified using Raman spectroscopy and XPS of rGO/10 wt % ANF, rGO-COOH/10 wt % ANF, and rGO-NH<sub>2</sub>/10 wt % ANF composite films. The characteristic D and G bands were observed for all three cases (Figure 4a, 4b and 4c). After thermal reduction the D/G ratio increased from 1.07 to 1.19 for rGO/10 wt % ANF, 1.15 to 1.23 for rGO-COOH/10 wt % ANF, and 1.01 to 1.03 for rGO-NH<sub>2</sub>/10 wt % ANF. The increased D/G ratio is derived from the smaller sp<sup>2</sup>-hybridized graphitic domains created upon reduction.<sup>[26]</sup>

The C/O ratio as obtained from XPS surveys (Figure S3) increased for all three cases, from 3.36 to 5.86 for rGO/10 wt % ANF, 2.89 to 4.52 for rGO-COOH/10 wt % ANF, and 4.57 to 7.62 for rGO-NH<sub>2</sub>/10 wt % ANF composite films. Figure 4d, 4e, and 4f show the C 1s high resolution spectra for the composite films before and after reduction. Before reduction, two distinct peaks were observed, corresponding to the sp<sup>2</sup>-hybridized carbon atoms (284.5 eV) and the oxygen-containing functional groups (286.1 eV). After thermal reduction, the peak assigned to the oxygen-containing functional groups disappeared, indicating

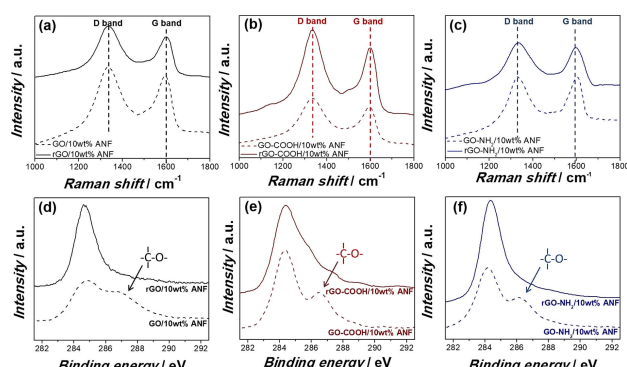


**Figure 4.** Raman spectra of a) GO/10 wt % ANF and rGO/10 wt % ANF, b) GO-COOH/10 wt % ANF and rGO-COOH/10 wt % ANF, and c) GO-NH<sub>2</sub>/10 wt % ANF and rGO-NH<sub>2</sub>/10 wt % ANF. High resolution XPS spectra for the C 1s peak for d) GO/10 wt % ANF and rGO/10 wt % ANF, e) GO-COOH/10 wt % ANF and rGO-COOH/10 wt % ANF, and f) GO-NH<sub>2</sub>/10 wt % ANF and rGO-NH<sub>2</sub>/10 wt % ANF.

the successful reduction.<sup>[27]</sup> XPS was also utilized to verify that the previously added functional groups remained grafted on GO even after reduction. For rGO-COOH/10 wt% ANF, the deconvolution of the C 1s peak was necessary to determine the ratio of the carboxylic acid ( $-\text{COOH}$ ) groups after reduction. The C 1s peak was deconvoluted to C–C (284.5 eV), C–N/C–O (286.1 eV), N=C=O (287.8 eV), O=C–OH (289 eV), and  $\pi\text{-}\pi$  interactions (291 eV).<sup>[16b]</sup> It was found that the amount of carboxylic acid ( $-\text{COOH}$ ) groups for rGO-COOH/10 wt% ANF (5.6%) was higher than rGO/10 wt% ANF (3.4%) (Figure S4 and Table S2). Moreover, 4.78 at% nitrogen was found in rGO-NH<sub>2</sub>/10 wt% ANF composite films, whereas only 1.25 at% nitrogen was apparent in the rGO/10 wt% ANF films, indicating that after reduction the amine functional groups remained grafted on GO. This was also confirmed by the XPS survey scan and high resolution N 1s peak for rGO-NH<sub>2</sub> sheets with no ANFs present (Figure S5).

#### 2.4. Hydrogen Bonding

We hypothesized that hydrogen bonding would be enhanced through the introduction of  $-\text{COOH}$  and  $-\text{NH}_2$  groups to the rGO sheets. Evidence of hydrogen bonding was confirmed from the high resolution N 1s spectra for the composite films (Figure S6). Two peaks were observed, the amide peak N=C=O at 399.9 eV and a second peak at 401.8 eV attributed to hydrogen bonding interactions between the ANF amide bonds and the oxygen-containing and/or amine groups of f-GO.<sup>[28]</sup> Moreover, an increase in the hydrogen bonding peak was apparent with functionalization, indicating the enhancement of hydrogen bonding interactions due to the addition of functional groups such as  $-\text{COOH}$  and  $-\text{NH}_2$ , confirming the extensive non-covalent interactions between rGO and ANFs.

#### 2.5. Mechanical Properties

To better understand the reinforcement effect, the mechanical properties of the rGO/ANF, rGO-COOH/ANF and rGO-NH<sub>2</sub>/ANF composite films were evaluated (Figure 5 and Table S3). Stress-strain curves typically exhibited three regimes: initial ( $E_i$ ), straightening ( $E_s$ ), and “elastic” ( $E_e$ ).<sup>[29]</sup> The initial and straightening regions are attributed to straightening geometric wrinkles and structural sliding of the reduced functionalized graphene sheets to adopt a more flattened structure. This behavior was apparent in the composite electrodes, as shown in Figure 5a.

The Young’s modulus, ultimate tensile strength, and toughness increased significantly with ANF content for all three cases, Figure 5b–d. The Young’s modulus of rGO/25 wt% ANF was  $9.9 \pm 2.0$  GPa, 115% higher than the Young’s modulus of pure rGO films ( $4.8 \pm 1.2$  GPa), as calculated from the “elastic” regimes. The ultimate tensile strength and toughness also increased by ~140% (from  $33 \pm 6.2$  to  $79 \pm 12.1$  MPa) and ~170% (from  $123 \pm 30.0$  to  $335 \pm 105$  kJ/m<sup>3</sup>), respectively. The enhancement of the mechanical properties is attributed to the increased hydrogen bonding and the  $\pi\text{-}\pi$  interactions that

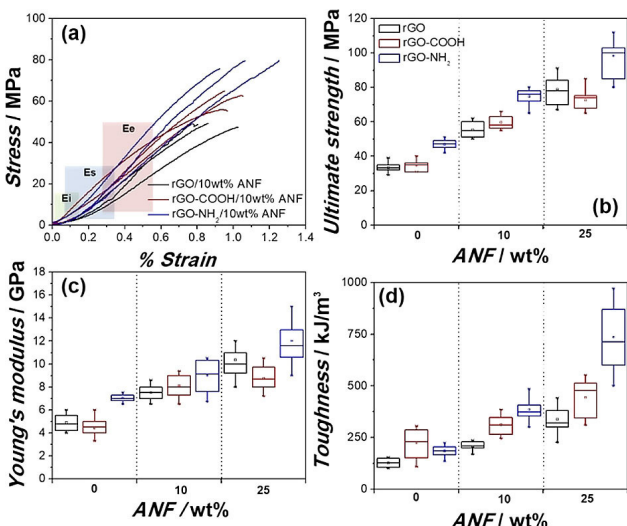


**Figure 5.** a) Typical stress-strain curves of rGO/10 wt % ANF, rGO-COOH/10 wt % ANF, and rGO-NH<sub>2</sub>/10 wt % ANF. Three regimes were observed: initial ( $E_i$ ), straightening ( $E_s$ ), and “elastic” ( $E_e$ ), labeled in green, blue, and red, respectively. Box plots of b) ultimate tensile strength, c) Young’s modulus, and d) toughness. The rectangular shapes extend from the first to the third quartile. The open squares represent the mean, whereas the lines inside the rectangular shapes represent the median. The whiskers indicate the maximum and minimum values. Each box corresponds to 12–15 data points.

facilitate load transfer between the reduced graphene oxide sheets and the 2D randomly oriented ANFs (Figure S4 and Figure S6). The reported values are comparatively lower from our previous studies since the previous tests were conducted at higher strain rates.<sup>[16b]</sup> As shown in Figure S7, f-rGO/ANF films exhibited strong strain rate dependency. At lower strain rates there is more time for the f-rGO sheets to slide and to reform hydrogen bonds, leading to lower stiffness and higher energy absorption.<sup>[24]</sup>

Next, the effect of functionalization with carboxylic acid ( $-\text{COOH}$ ) and amine ( $-\text{NH}_2$ ) functional groups was compared. rGO-COOH composite electrodes exhibited a slightly worse performance that resulted from two competing mechanisms. More specifically, the functionalization of GO with carboxylic acid ( $-\text{COOH}$ ) groups led to enhanced hydrogen bonding with the ANF amide groups but also led to a decrease in the stiffness of the functionalized GO sheets due to the introduction of defects, as shown previously from the Raman and XPS spectra.<sup>[30]</sup> Amine ( $-\text{NH}_2$ ) functionalized electrodes exhibited a better mechanical performance as a result of the enhanced hydrogen bonding interactions and not as harsh functionalization process creating fewer defects. The mechanical performance improved despite the wavier morphology (Figure 3). Wavier morphologies lead to lower in-plane stiffness and result in deteriorated mechanical performance.

The stiffness and ultimate strength increased by 18% ( $12.2 \pm 3.0$  GPa) and 24% ( $98 \pm 18$  MPa) for the rGO-NH<sub>2</sub>/25 wt% ANF electrodes, respectively, when compared to the non-functionalized electrodes of the same composition. Moreover, a remarkable increase in toughness was observed, with the toughness increasing by ~120% ( $732 \pm 232$  kJ/m<sup>3</sup>). The improvement in toughness can be attributed to two main

mechanisms. On the one hand, energy is dissipated in order to break the extensive hydrogen bonding between the ANFs and the f-rGOs at their interfaces, and some hydrogen bonds reform which then facilitate increased extensibility but continued increase in load bearing capacity.<sup>[24]</sup> Overall, the addition of ANFs and the amine ( $-\text{NH}_2$ ) functionalization of the graphene sheets (rGO vs. rGO–NH<sub>2</sub>/25 wt % ANF) led to increases in Young's modulus, ultimate tensile strength and toughness by ~150%, ~200%, and ~500%, respectively, Figure 5b-d.

Cyclic in plane tensile loading experiments were performed on all electrodes with a composition of 25 wt % ANF, Figure S8. An increase in the stiffness after 4 cycles was observed for all three types of samples. Repeated cyclic loading at small forces (0.15 Nt) under slow rates (0.2 Nt/min) allows the functionalized graphene sheets to slide and lock so that they "mechanically anneal" to the best structure.<sup>[29a]</sup> Stiffness of the non-functionalized electrodes did not change significantly for the same number of cycles, whereas the stiffness for rGO–COOH/25 wt % and rGO–NH<sub>2</sub>/25 wt % increased by 24% (10.9 GPa) and 44% (17.6 GPa), respectively, with cycling loading. These results show that small mechanical perturbations allow the hydrogen bonding interactions to reconfigure to adopt more favorable interactions, leading to enhanced stiffness. This mechanism explains the strain-stiffening behavior of the functionalized samples following cycling loading.

## 2.6. Electrochemical Properties

The electrochemical performance of the composite electrodes was evaluated using cyclic voltammetry and galvanostatic cycling. Two-electrode symmetric coin cells were assembled and 6 M KOH was used as the electrolyte. Cyclic voltammetry was performed at varying scan rates from 1 to 100 mV/s for each electrode type and the results are depicted in Figure 6a and Figure S9. The obtained cyclic voltammograms exhibited a rectangular shape indicating an ideal capacitive behavior where energy is stored through the formation of an electric double layer.<sup>[31]</sup>

The specific capacitance for each electrode was calculated at different scan rates, as shown in Figure 6b and Table S4. The specific capacitance decreased with the addition of ANF for all electrodes, since ANFs are electrochemically inactive. The highest values of specific capacitance for the rGO, rGO/10 wt % ANF and rGO/25wt %ANF electrodes were 216, 138 and 120 F/g at 1 mV/s, respectively. Moreover, functionalized composite electrodes exhibited diminished performance compared to non-functionalized electrodes. The lowest values of specific capacitance were obtained for the rGO–COOH electrodes with specific capacitances of 127, 104, and 98 F/g, for compositions of 0 wt %, 10 wt %, and 25 wt % ANF at 1 mV/s, respectively. rGO–NH<sub>2</sub> composite electrodes exhibited a slightly better performance with specific capacitances of 126, 116, and 104 F/g for the same compositions at 1 mV/s. The decrease in specific capacitance can be attributed to the introduction of defects during the functionalization step.

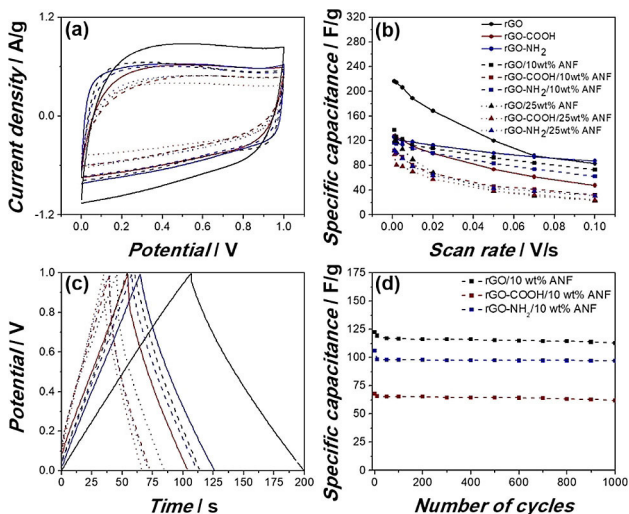


**Figure 6.** a) CV curves of rGO, rGO–COOH and rGO–NH<sub>2</sub> composite electrodes at 20 mV/s. b) Specific capacitance vs. scan rate. c) Galvanostatic charge/discharge curves of rGO, rGO–COOH and rGO–NH<sub>2</sub> composite electrodes at a current density of 0.5 A/g. The legend in (b) also applies to (a) and (c). d) Cycling behavior of rGO, rGO–COOH, and rGO–NH<sub>2</sub> composite electrodes up to 1000 cycles at 0.5 A/g.

Galvanostatic cycling was also performed at 0.5 A/g, Figure 6c and Table S5. The galvanostatic charge/discharge tests were in agreement with the results obtained by cyclic voltammetry, with a decreasing specific capacitance with ANF content. The specific capacitances were 187, 122, and 82 F/g for rGO, rGO/10 wt % ANF, and rGO/25 wt % ANF electrodes, respectively. Whereas, the electrodes with the same compositions for the rGO–COOH case exhibited specific capacitances of 98, 68, and 60 F/g. Similarly, rGO–NH<sub>2</sub>, composite electrodes had specific capacitances of 122, 106, and 62 F/g. The *iR* drop was 70 mV for rGO/10 wt % ANF, 180 mV for rGO–COOH/10 wt % ANF, and 80 mV for rGO–NH<sub>2</sub>/10 wt %, following the same trend with the specific capacitance. Furthermore, prolonged cycling up to 1000 cycles was performed on the composite electrodes containing 10 wt % ANF, Figure 6d. All electrodes exhibited excellent stability as a result of the extensive hydrogen bonding. The specific capacitance of the rGO/10 wt % ANF electrode retained 92% of the initial specific capacitance after 1000 cycles. In comparison, the rGO–COOH/10 wt % ANF and rGO–NH<sub>2</sub>/10 wt % ANF retained 90% and 92% of the initial capacitance.

Figure S10 shows a Ragone plot that summarizes specific energy vs. specific power and energy density vs. power density as calculated from the galvanostatic charge/discharge tests for different current densities (0.2, 0.5, 1, and 2 A/g). Table S6 provides estimated electrode densities used to calculate these performance metrics. rGO electrodes (no ANFs) exhibited the highest specific energy for a given specific power. Notably, rGO–NH<sub>2</sub> (no ANFs) exhibited the highest energy density for a given power density because of the higher mass density of the rGO–NH<sub>2</sub> electrode. Generally, as ANF content increased, energy and power decreased; also, –NH<sub>2</sub> functionalization was superior to –COOH functionalization in terms of energy and power.

## 2.7. Multifunctionality

In order to visualize the multifunctional nature of the composite electrodes, an Ashby plot of the specific capacitance vs. ultimate strength of our results compared against other free-standing structural electrodes from the literature was constructed, Figure 7a and Table S7. The plot includes rGO aerogels, multi- and single-walled carbon nanotube (MWCNT and SWCNT) buckypapers, rGO/MnO<sub>2</sub>, rGO/MnO<sub>2</sub>/CNTs, poly-pyrrole (Ppy)/rGO, rGO-cellulose, rGO-polyaniline (PANI), SWCNT-Ppy-cyanate ester (CE), and rGO/CNT wire shaped composites.<sup>[16b,32]</sup> It can be observed that f-rGO/ANF electrodes exhibit a good combination of mechanical and electrochemical properties compared to other carbon-based structural electrodes. Even though, other electrodes, such as rGO/MnO<sub>2</sub>/CNT, Ppy/rGO, and SWCNT-Ppy-CE, displayed higher specific capacitance, the f-rGO/ANF electrodes exhibited higher ultimate tensile strength values. This is attributed to the extensive hydrogen bonding and  $\pi$ - $\pi$  interactions between the functionalized graphene sheets and ANFs (Figure S4 and Figure S6). Moreover, a trade-off between the mechanical and electro-

chemical properties is apparent. Specifically, increasing the ANF content improves the mechanical properties at the expense of the specific capacitance. It was also observed that the functionalization of the graphene oxide sheets affected this trade-off. More specifically, the rGO-NH<sub>2</sub>/ANF electrodes displayed enhanced mechanical performance due to the enhanced hydrogen bonding at the cost of the electrochemical performance because of the introduction of defects in the rGO sheets.

This trade-off can be better demonstrated by the multifunctional efficiency.<sup>[33]</sup> The multifunctional efficiency ( $n_{mf}$ ) is expressed as the summation of the energy ( $n_e$ ) and the structural ( $n_s$ ) efficiencies:

$$n_{mf} \equiv n_e + n_s > 1 \text{ where } n_e = \frac{\bar{T}_{mf}}{\bar{T}} \text{ and } n_s = \frac{\bar{E}_{mf}}{\bar{E}} \text{ or } n_s = \frac{\bar{UTS}_{mf}}{\bar{UTS}}$$
(1)

where  $\bar{T}$ ,  $\bar{E}$ , and  $\bar{UTS}$  are the specific energy, specific Young's modulus, and specific tensile strength of the monofunctional/conventional device, respectively, whereas  $\bar{T}_{mf}$ ,  $\bar{E}_{mf}$ , and  $\bar{UTS}_{mf}$  are the same quantities for the multifunctional system. In order to obtain savings in mass and volume the multifunctional efficiency ( $n_{mf}$ ) should be higher than unity.<sup>[33]</sup>

Here, the multifunctional efficiency was calculated using carbon aerogel (specific energy 12.5 Wh/kg) as the monofunctional energy storage material.<sup>[34]</sup> The structural efficiency was calculated for four different monofunctional structural materials: carbon fiber reinforced epoxy (specific Young's modulus of 44 GPa cm<sup>3</sup>/g and specific tensile strength of 375 MPa cm<sup>3</sup>/g),<sup>[35]</sup> aluminum (specific Young's modulus of 25.5 GPa cm<sup>3</sup>/g and specific tensile strength of 153.7 MPa cm<sup>3</sup>/g),<sup>[36]</sup> steel (specific Young's modulus of 26.5 GPa cm<sup>3</sup>/g and specific tensile strength of 88.5 MPa cm<sup>3</sup>/g),<sup>[37]</sup> and epoxy (specific Young's modulus of 2.8 GPa cm<sup>3</sup>/g and specific tensile strength of 60 MPa cm<sup>3</sup>/g).<sup>[16b]</sup> All four materials are currently used in automobile and aerospace applications. Figure 7b demonstrates that the f-rGO/ANF multifunctional electrodes have the potential to be employed in such applications as multifunctional/structural electrodes leading to mass and volume savings for steel or epoxy.

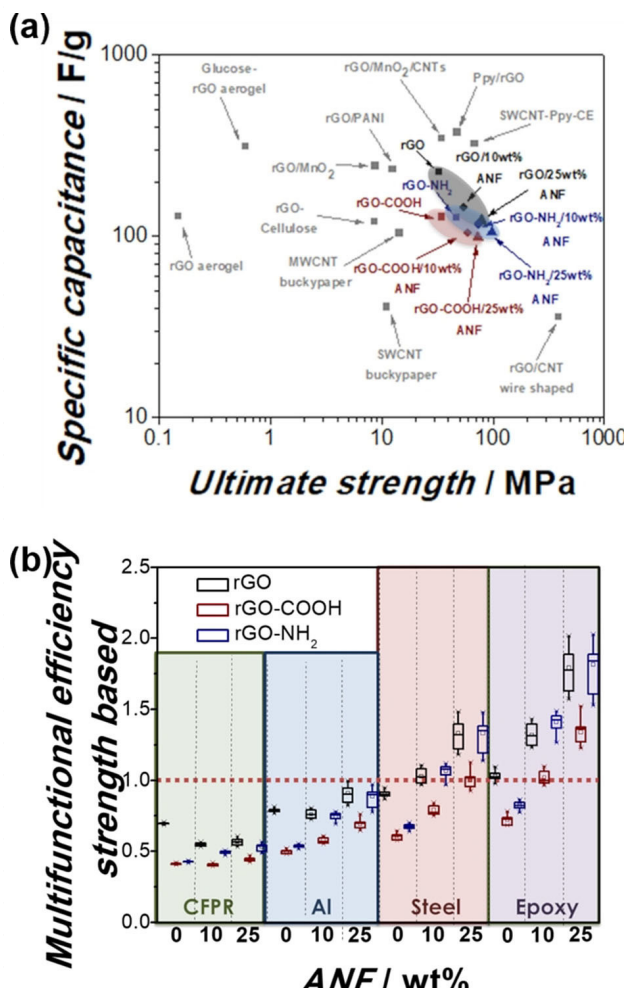


**Figure 7.** a) Ashby plot of specific capacitance vs. ultimate strength. Table S7 provides more detail. b) Multifunctional efficiency (strength based) for four different structural benchmark materials.

## 3. Conclusion

Structural electrodes for supercapacitors containing ANFs and reduced functionalized graphene sheets were fabricated using vacuum filtration to exploit the extensive hydrogen bonding interactions between the ANF amide groups and the -COOH or -NH<sub>2</sub> groups on f-rGO through interfacial engineering. The addition of ANFs, as well as the functionalization of GO led to a compromise between the mechanical and electrochemical properties. An improvement of 115%, 140%, and 170% in Young's modulus, ultimate tensile strength, and toughness was achieved by the incorporation of ANF to the pure rGO composite electrodes, whereas the specific capacitance decreased (~45%). Functionalization with -NH<sub>2</sub> groups also led to an enhancement in the mechanical properties, with the Young's

modulus, ultimate tensile strength, and toughness increasing by 18%, 24%, and 120%, compared to pure rGO/ANF films. In all cases, the capacitance was affected by the functionalization. This was attributed to two competing mechanisms, the enhanced hydrogen bonding interactions vs. the introduction of defects during functionalization. The introduction of defects disrupts the  $sp^2$ -hybridized network of carbon atoms leading to lower f-rGO sheet stiffness and conductivity. Overall, the addition of ANF and the amine ( $-NH_2$ ) functionalization of the graphene oxide sheets (rGO vs. rGO-NH<sub>2</sub>/25 wt% ANF) gave the best mechanical improvement; Young's modulus, ultimate tensile strength and toughness increased by 150%, 200%, and 500%, respectively. The f-rGO/ANF supercapacitors exhibited a good combination of mechanical and electrochemical properties compared to other state-of-the-art carbon-based structural electrodes. This was further demonstrated by the multifunctional efficiency that was above unity, suggesting the potential of these structural electrodes in real-life applications, such as in the transportation, satellites, or aircraft.

## Experimental Section

### Materials

Graphite (SP-1) and Kevlar®69 thread were purchased from Bay Carbon and Thread Exchange, respectively. Dimethyl sulfoxide (DMSO), potassium permanganate, and sodium nitrate were purchased from Sigma Aldrich. Potassium hydroxide (KOH) was provided by Amresco. Hydrobromic acid (HBr) and ethylenediamine were purchased from BDH. Oxalic acid and carbon paper were purchased by Alfa Aesar. Microporous poly(propylene) separator (Celgard 3501) was purchased from Celgard.

### Preparation of the Aramid Nanofiber (ANF) and Graphene Oxide Dispersion

In dimethyl sulfoxide DMSO (500 ml), Kevlar®69 thread (1 g) and potassium hydroxide KOH (1.5 g) were added, followed by magnetic stirring for 14 days at room temperature.<sup>[6a]</sup> A dark red dispersion of ANF/DMSO (2 mg/ml) was obtained. Graphene oxide was prepared using the modified Hummers method.<sup>[38]</sup> More specifically, in a cold solution of H<sub>2</sub>SO<sub>4</sub> (120 ml), graphite powder (3 g) and NaNO<sub>3</sub> (2.5 g) were added. The mixture was stirred in an ice water bath for 5 hours. Next, KMnO<sub>4</sub> (15 g) was gradually added while the temperature was kept below 20 °C. Then, the mixture was heated at 35 °C for 2 h followed by the addition of deionized water (250 ml). The mixture was diluted further with the addition of deionized water (700 ml) and stirred for 30 min. Subsequently, 30 wt% H<sub>2</sub>O<sub>2</sub> (20 ml) was added and the color of the mixture turned black from green. Finally, the mixture was washed with 5 wt% HCl solution, filtered through a Whatman filter paper (55 mm diameter and 2.5 μm pore size) and dialyzed to remove metal ions and acids. The resulting dispersion was dried overnight, and graphite oxide powder was obtained. The powder was dissolved in deionized water and ultrasonicated to exfoliate the graphene oxide sheets. Graphene oxide was then dispersed in water (2 mg/ml) and further sonicated. Solvent exchange was used to obtain a GO/DMSO dispersion.

### Preparation of Functionalized Graphene Oxide (f-GO)

To obtain GO functionalized with carboxylic acid groups ( $-COOH$ ), GO (100 mg) was dispersed in de-ionized water (50 ml) and hydrobromic acid (6.67 ml) was added. The mixture was stirred vigorously for 24 h at room temperature. Then, oxalic acid (2 g) was added under magnetic stirring for 4 h at room temperature. The dispersion was filtrated, dried at 60 °C under vacuum overnight and re-dispersed in DMSO (1 mg/ml).<sup>[18]</sup> To obtain GO functionalized with amine groups ( $-NH_2$ ), ethylenediamine (300 mg) was dissolved in ethanol (50 ml) and added dropwise to an aqueous GO (100 ml of 2 mg/ml) dispersion. The mixture was stirred vigorously at room temperature for 24 h. The functionalized GO was isolated by filtration and washed three times with 1:1 (v/v) ethanol/water. The precipitate was dried in vacuum overnight at 60 °C and re-dispersed in DMSO (1 mg/ml).<sup>[20a,39]</sup>

### Preparation of f-GO/ANF Composite Film

Vacuum-assisted filtration was used to fabricate the f-GO/ANF composite films. The total mass of the film was held constant at 40 mg. ANF/DMSO dispersion (0.2 mg/ml) and f-GO/DMSO dispersion (1 mg/ml) at the desired amounts were stirred for 1 h. Then deionized water was added to the mixture and stirred further for 2 h at 80 °C in order to reprotoenate the amide groups of the ANFs. The mixture was vacuum-filtered on nylon filter membrane (47 mm diameter, 0.2 μm pore size). The resulting composite films were then rinsed with water, air-dried and dried at 80 °C in vacuum for 3 days. The films were thermally reduced at 200 °C in vacuum for 2 h to yield reduced f-GO/ANF composite films. During the reduction step, films were placed between glass slides and heavy tiles to prevent bubble formation. Finally, the free-standing films were cut into rectangular strips (2 mm × 20 mm) using a razor blade for tensile testing and circles of 16 mm in diameter by punching the films for electrochemical testing.

### Materials Characterization

The morphology and thickness of the composite films were investigated using scanning electron microscopy (SEM) (JSM-7500F, JEOL and Helios). Raman spectra were obtained by a Horiba Jobin Yvon spectrometer with 514 nm excitation and XPS spectra by an Omicron ESCA Probe (Omicron Nanotechnology) with a monochromatized Mg Ka radiation ( $h\nu = 1253.6$  eV). XPS survey scans were performed with an analyzer pass energy of 100–1100 eV (1.0 eV steps, 50 ms dwell time), while high resolution scans of carbon (C 1s) and nitrogen (N 1s) were performed with a pass energy of 150 eV (0.05 eV steps, 200 ms dwell time). All spectra were calibrated with the C 1s photoemission peak for  $sp^2$ -hybridized carbons at 284.5 eV and the FWHM was constrained. Curve fitting of C 1s and N 1s spectra was conducted using a Gaussian-Lorentzian peak shape after Shirley-type background correction.

### Mechanical Characterization

Static uniaxial in-plane tensile tests and cyclic loading were performed using a dynamic mechanical analyzer (DMA Q800, TA Instruments). A film tension clamp with a compliance of 1.8 μm/N was used. The tensile tests were conducted in controlled strain rate mode with a preload force of 0.02 N and a strain ramp rate of 0.1%/min. The toughness was calculated from the area underneath the stress-strain curves up to the point of fracture. All tensile tests were conducted in room conditions (temperature: 22–25 °C and humidity: 40–50%).

## Electrochemical Characterization

Two electrode symmetric coin cells were used to evaluate the electrochemical performance of the composite films. The coin cells consisted of a top and bottom stainless steel covering, two current collectors (carbon paper), two electrodes, the electrolyte (6 M KOH), two spacers, a spring, and the separator (polypropylene). The electrochemical tests (cyclic voltammetry and galvanostatic charge/discharge) were conducted using a Gamry Potentiostat/Galvanostat Instrument (Gamry Interface 1000, Gamry Instruments). Cyclic voltammetry was conducted at various scan rates in a potential window of 0–1 V. The specific capacitance (F/g) of the electrode was calculated from cyclic voltammetry curve using the equation,  $C = 2 \frac{\int_{V-}^{V+} IdV}{v \cdot \Delta V \cdot M}$ , where  $I$  is the current (A),  $V+$  and  $V-$  the high and low voltage (V) cut-off respectively,  $M$  the total mass (g) of the two electrodes,  $\Delta V$  the potential window, and  $v$  the scan rate. Galvanostatic charge/discharge tests were performed at variant current densities (A/g). The specific capacitance was calculated by the equation,  $C = \frac{4 \cdot I \cdot \Delta t}{M \cdot \Delta V}$ , where  $\Delta t$  is the discharge time (s).

## Acknowledgements

The authors acknowledge the TAMU Materials Characterization Facility. JL acknowledges the William and Ruth Neely Faculty Fellowship. This work was supported by Air Force Office of Scientific Research Grant No. FA9550-16-1-0230. The authors thank Prof. Micah Green of Texas A&M University and Prof. Haleh Ardebili of University of Houston for their helpful discussions.

## Conflict of interest

The authors declare no conflict of interest.

**Keywords:** aramid nanofibers • functionalized graphene • multifunctional electrodes • structural energy and power • supercapacitors

- [1] a) L. E. Asp, E. S. Greenhalgh, *Compos. Sci. Technol.* **2014**, *101*, 41; b) N. Shirshova, H. Qian, M. S. P. Shaffer, J. H. G. Steinke, E. S. Greenhalgh, P. T. Curtis, A. Kucernak, A. Bismarck, *Composites Part A: Applied Science and Manufacturing* **2013**, *46*, 96; c) H. Peng, G. Qian, N. Li, Y. Yao, T. Lv, S. Cao, T. Chen, *Adv. Sci. O.* **1800784**.
- [2] a) H. Nishide, K. Oyizu, *Science* **2008**, *319*, 737; b) M. F. El-Kady, V. Strong, S. Dubin, R. B. Kaner, *Science* **2012**, *335*, 1326; c) X. Wang, X. Lu, B. Liu, D. Chen, Y. Tong, G. Shen, *Adv. Mater.* **2014**, *26*, 4763; d) L. Wen, F. Li, H.-M. Cheng, *Adv. Mater.* **2016**, *28*, 4306.
- [3] W. Liu, M.-S. Song, B. Kong, Y. Cui, *Adv. Mater.* **2017**, *29*, 1603436.
- [4] a) J. F. Snyder, E. B. Gienger, E. D. Wetzel, *J. Compos. Mater.* **2015**, *49*, 1835; b) J. F. Snyder, R. H. Carter, E. D. Wetzel, *Chem. Mater.* **2007**, *19*, 3793; c) J. Hagberg, S. Leijonmarck, G. Lindbergh, *J. Electrochem. Soc.* **2016**, *163*, A1790; d) M. Yousa, H. T. H. Shi, Y. Wang, Y. Chen, Z. Ma, A. Cao, H. E. Naguib, R. P. S. Han, *Adv. Energy Mater.* **2016**, *6*, 1600490; e) L. Huang, D. Santiago, P. Loyselle, L. Dai, *Small* **0**, 1800879.
- [5] a) H. D. Wagner, R. A. Vaia, *Mater. Today* **2004**, *7*, 38; b) S.-Y. Fu, X.-Q. Feng, B. Lauke, Y.-W. Mai, *Composites Part B: Engineering* **2008**, *39*, 933; c) V. Palermo, I. A. Kinloch, S. Ligi, N. M. Pugno, *Adv. Mater.* **2016**, *28*, 6232; d) S. Chhetri, N. C. Adak, P. Samanta, P. K. Mallisetty, N. C. Murmu, T. Kuila, *J. Appl. Polym. Sci.* **2018**, *135*, 46124.
- [6] a) M. Yang, K. Cao, L. Sui, Y. Qi, J. Zhu, A. Waas, E. M. Arruda, J. Kieffer, M. D. Thouless, N. A. Kotov, *ACS Nano* **2011**, *5*, 6945; b) K. Cao, C. P.

- Siepermann, M. Yang, A. M. Waas, N. A. Kotov, M. D. Thouless, E. M. Arruda, *Adv. Funct. Mater.* **2013**, *23*, 2072.
- [7] a) P. N. B. Reis, J. A. M. Ferreira, P. Santos, M. O. W. Richardson, J. B. Santos, *Compos. Struct.* **2012**, *94*, 3520; b) D. Tanner, J. A. Fitzgerald, B. R. Phillips, *Angewandte Chemie Int. Ed. Engl.* **1989**, *28*, 649.
- [8] a) J. Zhu, W. Cao, M. Yue, Y. Hou, J. Han, M. Yang, *ACS Nano* **2015**, *9*, 2489; b) J. Fan, Z. Shi, L. Zhang, J. Wang, J. Yin, *Nanoscale* **2012**, *4*, 7046; c) J. Fan, Z. Shi, M. Tian, J. Yin, *RSC Adv.* **2013**, *3*, 17664; d) Y. Guan, W. Li, Y. L. Zhang, Z. Q. Shi, J. Tan, F. Wang, Y. H. Wang, *Compos. Sci. Technol.* **2017**, *144*, 193; e) Q. Kuang, D. Zhang, J. C. Yu, Y.-W. Chang, M. Yue, Y. Hou, M. Yang, *J. Phys. Chem. C* **2015**, *119*, 27467; f) Y. Ming, C. Keqin, Y. Bongjun, M. D. Thouless, W. Anthony, M. A. Ellen, A. K. Nicholas, *J. Compos. Mater.* **2015**, *49*, 1873.
- [9] J. Lin, S. H. Bang, M. H. Malakooti, H. A. Sodano, *ACS Appl. Mater. Interfaces* **2017**, *9*, 11167.
- [10] a) Y. Li, G. Ren, Z. Zhang, C. Teng, Y. Wu, X. Lu, Y. Zhu, L. Jiang, *J. Mater. Chem. A* **2016**, *4*, 17324; b) J. Li, W. Tian, H. Yan, L. He, X. Tuo, *J. Appl. Polym. Sci.* **2016**, *133*, n/a; c) S.-O. Tung, S. Ho, M. Yang, R. Zhang, N. A. Kotov, *Nat. Commun.* **2015**, *6*, 6152; d) S. Hu, S. Lin, Y. Tu, J. Hu, Y. Wu, G. Liu, F. Li, F. Yu, T. Jiang, *J. Mater. Chem. A* **2016**, *4*, 3513; e) J. Lyu, M. D. Hammig, L. Liu, L. Xu, H. Chi, C. Uher, T. Li, N. A. Kotov, *Appl. Phys. Lett.* **2017**, *111*, 161901; f) J. Lyu, X. Wang, L. Liu, Y. Kim, E. K. Tanyi, H. Chi, W. Feng, L. Xu, T. Li, M. A. Noginov, C. Uher, M. D. Hammig, N. A. Kotov, *Adv. Funct. Mater.* **2016**, *26*, 8435.
- [11] a) A. K. Geim, K. S. Novoselov, *Nat. Mater.* **2007**, *6*, 183; b) K. S. Novoselov, A. K. Geim, S. V. Morozov, D. Jiang, Y. Zhang, S. V. Dubonos, I. V. Grigorieva, A. A. Firsov, *Science* **2004**, *306*, 666.
- [12] a) M. D. Stoller, S. Park, Y. Zhu, J. An, R. S. Ruoff, *Nano Lett.* **2008**, *8*, 3498; b) H. Gwon, H.-S. Kim, K. U. Lee, D.-H. Seo, Y. C. Park, Y.-S. Lee, B. T. Ahn, K. Kang, *Energy Environ. Sci.* **2011**, *4*, 1277.
- [13] a) W. Gao, L. B. Alemany, L. Ci, P. M. Ajayan, *Nat. Chem.* **2009**, *1*, 403; b) O. C. Compton, S. T. Nguyen, *Small* **2010**, *6*, 711; c) D. Li, M. B. Müller, S. Gilje, R. B. Kaner, G. G. Wallace, *Nat. Nanotechnol.* **2008**, *3*, 101.
- [14] a) Y. He, W. Chen, X. Li, Z. Zhang, J. Fu, C. Zhao, E. Xie, *ACS Nano* **2013**, *7*, 174; b) G. Wang, X. Sun, F. Lu, H. Sun, M. Yu, W. Jiang, C. Liu, J. Lian, *Small* **2012**, *8*, 452; c) Z. Weng, Y. Su, D.-W. Wang, F. Li, J. Du, H.-M. Cheng, *Adv. Energy Mater.* **2011**, *1*, 917.
- [15] a) D.-W. Wang, F. Li, J. Zhao, W. Ren, Z.-G. Chen, J. Tan, Z.-S. Wu, I. Gentle, G. Q. Lu, H.-M. Cheng, *ACS Nano* **2009**, *3*, 1745; b) A. Sumboja, C. Y. Foo, X. Wang, P. S. Lee, *Adv. Mater.* **2013**, *25*, 2809.
- [16] a) S. R. Kwon, M. B. Elkins, J. D. Batteas, J. L. Lutkenhaus, *ACS Appl. Mater. Interfaces* **2017**, *9*, 17125; b) S. R. Kwon, J. Harris, T. Zhou, D. Loufakis, J. G. Boyd, J. L. Lutkenhaus, *ACS Nano* **2017**, *11*, 6682.
- [17] a) H. He, J. Klinowski, M. Forster, A. Lerf, *Chem. Phys. Lett.* **1998**, *287*, 53; b) D. R. Dreyer, S. Park, C. W. Bielawski, R. S. Ruoff, *Chem. Soc. Rev.* **2010**, *39*, 228.
- [18] a) Y. Liu, R. J. Deng, Z. Wang, H. T. Liu, *J. Mater. Chem.* **2012**, *22*, 13619; b) X. Fang, X. Liu, Z.-K. Cui, J. Qian, J. Pan, X. Li, Q. Zhuang, *J. Mater. Chem. A* **2015**, *3*, 10005.
- [19] K. P. Loh, Q. Bao, P. K. Ang, J. Yang, *J. Mater. Chem.* **2010**, *20*, 2277.
- [20] a) A. B. Bourlino, D. Gournis, D. Petridis, T. Szabó, Á. Szeri, I. Dékány, *Langmuir* **2003**, *19*, 6050; b) J.-I. Yan, G.-j. Chen, J. Cao, W. Yang, B.-h. Xie, M.-b. Yang, *Carbon* **2013**, *52*, 624.
- [21] a) J. Shen, Y. Hu, M. Shi, X. Lu, C. Qin, C. Li, M. Ye, *Chem. Mater.* **2009**, *21*, 3514; b) F. Tuinstra, J. L. Koenig, *J. Chem. Phys.* **1970**, *53*, 1126.
- [22] K. N. Kudin, B. Ozbas, H. C. Schniepp, R. K. Prud'homme, I. A. Aksay, R. Car, *Nano Lett.* **2008**, *8*, 36.
- [23] D. Yang, A. Velamakanni, G. Bozoklu, S. Park, M. Stoller, R. D. Piner, S. Stankovich, I. Jung, D. A. Field, C. A. Ventrice, R. S. Ruoff, *Carbon* **2009**, *47*, 145.
- [24] L. Xu, X. Zhao, C. Xu, N. A. Kotov, *Adv. Mater.* **2018**, *30*, 1703343.
- [25] a) J. R. Potts, D. R. Dreyer, C. W. Bielawski, R. S. Ruoff, *Polymer* **2011**, *52*, 5; b) M. Ghislandi, E. Tkalya, S. Schillinger, C. E. Koning, G. de With, *Compos. Sci. Technol.* **2013**, *80*, 16.
- [26] G. Eda, F. Fanchini, M. Chhowalla, *Nat. Nanotechnol.* **2008**, *3*, 270.
- [27] S. Park, J. An, J. R. Potts, A. Velamakanni, S. Murali, R. S. Ruoff, *Carbon* **2011**, *49*, 3019.
- [28] H. R. Byon, S. W. Lee, S. Chen, P. T. Hammond, Y. Shao-Horn, *Carbon* **2011**, *49*, 457.
- [29] a) S. Park, K.-S. Lee, G. Bozoklu, W. Cai, S. T. Nguyen, R. S. Ruoff, *ACS Nano* **2008**, *2*, 572; b) D. A. Dikin, S. Stankovich, E. J. Zimney, R. D. Piner, G. H. B. Dommett, G. Evmelenko, S. T. Nguyen, R. S. Ruoff, *Nature* **2007**, *448*, 457.
- [30] G. Wang, Z. Dai, L. Liu, H. Hu, Q. Dai, Z. Zhang, *ACS Appl. Mater. Interfaces* **2016**, *8*, 22554.

- [31] M. D. Stoller, R. S. Ruoff, *Energy Environ. Sci.* **2010**, *3*, 1294.
- [32] a) Y. Cheng, S. Lu, H. Zhang, C. V. Varanasi, J. Liu, *Nano Lett.* **2012**, *12*, 4206; b) W. S. V. Lee, E. Peng, D. C. Choy, J. M. Xue, *J. Mater. Chem. A* **2015**, *3*, 19144.
- [33] a) D. J. O. Brien, D. M. Baechle, E. D. Wetzel, *J. Compos. Mater.* **2011**, *45*, 2797; b) D. J. O'Brien, D. M. Baechle, E. D. Wetzel, **2010**, DOI: 10.1115/SMASIS2010-3873215; c) D. Baechle, D. O'Brien, E. Wetzel, presented at Proc. of SPIE Vol.
- [34] a) L. L. Zhang, X. S. Zhao, *Chem. Soc. Rev.* **2009**, *38*, 2520; b) D. Qu, H. Shi, *J. Power Sources* **1998**, *74*, 99.
- [35] C. Soutis, *Prog. Aerosp. Sci.* **2005**, *41*, 143.
- [36] K. Suganuma, T. Fujita, N. Suzuki, K. Niihara, *J. Mater. Sci. Lett.* **1990**, *9*, 633.
- [37] H. Ledbetter, *J. Appl. Phys.* **1981**, *52*, 1587.
- [38] W. S. Hummers, R. E. Offeman, *J. Am. Chem. Soc.* **1958**, *80*, 1339.
- [39] V. Georgakilas, M. Otyepka, A. B. Bourlinos, V. Chandra, N. Kim, K. C. Kemp, P. Hobza, R. Zboril, K. S. Kim, *Chem. Rev.* **2012**, *112*, 6156.

---

Manuscript received: December 4, 2018

Revised manuscript received: January 27, 2019

Accepted manuscript online: January 30, 2019

Version of record online: February 20, 2019

---